PHOTONICS Research

Single-cell detection by enhancement of fluorescence in waveguides for cancer diagnosis and therapy

HAILANG DAI,[1,†] 🄳 HONGRUI SHAN,[1,†] ZHANGCHI SUN,[2,3,†] DAOPENG DAI,[4] YUXI SHANG,[1] ZHUANGQI CAO,[1] AND XIANFENG CHEN[1,5,*]

[1]State Key Laboratory of Advanced Optical Communication Systems and Networks, School of Physics and Astronomy, Shanghai Jiao Tong University, Shanghai 200240, China
[2]Zhejiang Rongjun Hospital, Jiaxing 314000, China
[3]School of Pharmacy, Shanghai Jiao Tong University, Shanghai 200240, China
[4]Department of Cardiology, Ruijin Hospital, Shanghai Jiao Tong University School of Medicine, Shanghai 200240, China
[5]Collaborative Innovation Centre of Light Manipulations and Applications, Shandong Normal University, Jinan 250358, China
*Corresponding author: xfchen@sjtu.edu.cn

Cancer is one of the most common diseases to threaten human health. If individuals are diagnosed with malignant tumors via a single cell, medical workers are greatly advantageous to early diagnose and intervene in malignant tumors therapy. In this paper, we propose a fluorescence detection map to rapidly distinguish whether the chromosomes of a cell are normal or abnormal by detecting the fluorescent intensity of a single cell. Herein, we draw a map from a single cell with an abnormal number of chromosomes that is monitored in real time. Moreover, this way offers precise and prompt detection of the surviving of cancer cells at or near the site of the tumor after treatments for cancer, which can achieve personalized cancer diagnosis and therapy. Therefore, cancer recurrences and metastasis can be effectively identified, utilizing this ultrasensitive detection method of an abnormal chromosome number.   © 2021 Chinese Laser Press

1. INTRODUCTION

Malignant tumors are common and lethal [1–3]. Recurrence and metastasis are the two main problems with cancer therapy [4]. Currently, treatments for cancer can be separated into three categories: radiation, surgical removal of a tumor, and chemotherapy [5,6]. However, the cancer can recur at or near the site of the tumor or distant points [7]. Cancer recurrence can be a combination of various factors. One of the main causes is that incomplete cancer treatment results in the surviving of cancer cells in the patient's body.

The early diagnosis and adjuvant treatment could improve the chance of killing any remaining cancer cells and reduce the risk of relapse. Early detection of recurrence during the follow-up is associated with improved survival rates in patients with early-stage cancer [8] regardless of whether they have received adjustment therapy [9]. The biomarker now is used as the standard of cure, in which a carcinoembryonic antigen (CEA) [10] has limited sensitivity. Computed tomography (CT) [11] imaging improves the detection of recurrences, but it is associated with radiation exposure and also a high false-positive rate.

Nanomedicine aims to improve the biodistribution and the target site accumulation of systemically applied chemotherapeutics. Organic dyes [12], nanoparticles [13], semiconductors [14], quantum dots [15], and other nanomaterials [16] have been extensively investigated. These systems offer a novel combination of tunable photoluminescence, excellent photostability, biocompatibility, and chemical inertness. Moreover, many routinely used (chemo)therapeutic agents suffer from poor pharmacokinetics and biodistribution. Because of their low molecular weight, for instance, intravenously administered anticancer drugs are generally rapidly cleared from the circulation (by means of renal filtration), and they do not accumulate well in tumor cells. Strong photobleaching and inferior thermal stability of conventional organic dyes as well as the cytotoxicity of nanoparticles and semiconductor quantum dots hinder practical applications. The detection of an abnormal chromosome number in cancer cells [16–19] is a signal to successful cancer treatment. Normal cells are diploid, and the cancer cell is nondiploid because of spontaneous mitotic chromosome nondisjunction in the cancer cell [16]. Different intensities of fluorescence can be detected by optical techniques due to the different chromosome number.

In this paper, we provide a fluorescence detection map drawn by a strong coupling waveguide, hollow-core metal-cladding optofluidic waveguide, to detect the intensity of fluorescence from a single cell and analyze the chromosome number in the cell. Our strategy is described below. First, cells with DAPI-stained chromosomes are injected into a sample channel one by one. Meanwhile, the specific ultrahigh-order modes (UOMs) in the guiding layer of the waveguide are excited by adjusting the incident angle of light to fulfill the phase-match condition [20]. Second, when cells are injected into the channel, the intensity of the fluorescence is significantly changed and monitored. Fluorescent faculae are found in the coupled area of the light spot, and the fluorescence intensity of the chromosomes can be measured at a fixed angle [21–23]. Finally, the leaked fluorescence of the single cell through the

coupling layer is collected and recorded. The fluorescence intensity is proportional to the number of chromosomes. By analyzing the intensity of the leaked fluorescence, we can draw a map to distinguish the number of the chromosomes from the single cell and detect whether it is normal or not. In this way, we precisely and promptly detect the reproductive cells of male mice, lung cancer cells, and surviving cancer cells after treatment of cancer by the three categories of therapy.

2. RESULTS

A. Map Setup with Lung Cancer Cell via Chromosome Fluorescence

In a previous study [24,25], the low intensity of the fluorescence can be detected by our strong coupling waveguide. Because the different fluorescent intensities correspond to
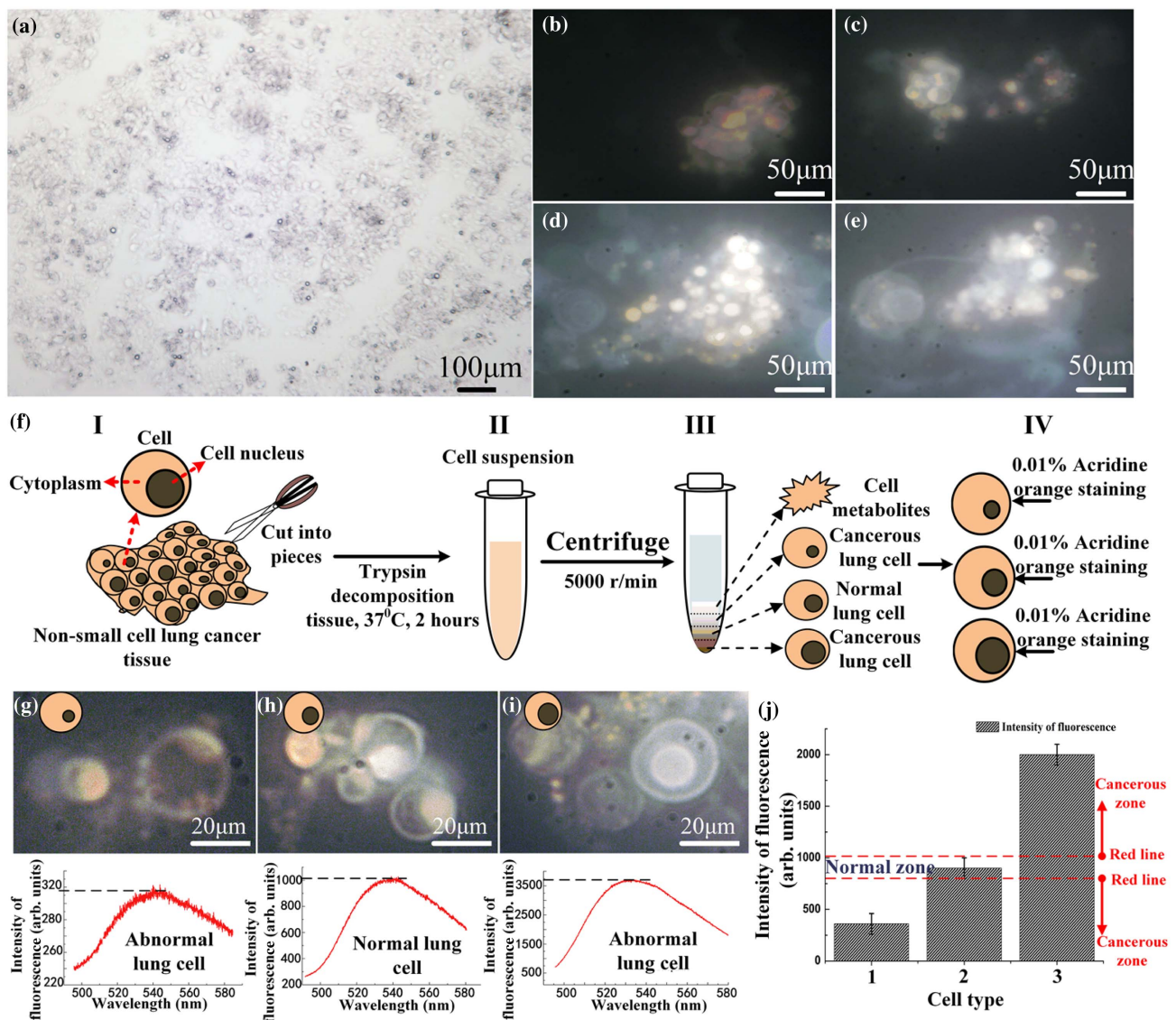

Fig. 1. Detection of cancer cells via chromosome fluorescence. (a) Nonsmall cell lung cancer (NSCLC) cell is examined under a microscope to confirm the diagnosis; cells (1×10^5 – 2×10^5 mL^{-1}) are seeded on normal slices. (b)–(e) Fluorescence images magnified 60 times for different cells by microscope; the chromosomes were stained by DAPI in cells. (f) Separation of different sizes and weights of cancer cells. (g)–(i) Normal and abnormal cell microscopic images show the detection of fluorescence intensity in our waveguide. (j) Drawing the map of cells which is distinguished according to the fluorescence intensity of normal and abnormal cells.

different chromosome numbers, it is possible to distinguish abnormalities by a cell's chromosome number. Thus, we used nonsmall cell lung cancer (NSCLC) cells from a 53-year-old male whose cancer had progressed on multiple prior lines of chemotherapy and epidermal growth factor receptor tyrosine kinase inhibitors; resistance biopsy was T790M+ without evidence of the C797S mutation. The biopsies were separated and processed as cell solutions. Figure 1(a) displays the section of NSCLC cells under a microscope. Different cancer cell lines with DAPI stained chromosomes are shown in Figs. 1(b)–1(e) under a 60-fold microscope. Figure 1(f) illustrates a brief flow diagram of the separation of different cells. The separations of cells stained by DAPI are based on their sizes. The cells are divided into three groups based on their number of chromosomes. A normal group indicates two sets of chromosomes (all human beings have 46 chromosomes in 23 matching pairs [26]), whereas the abnormal group contains 23, 69, or many more chromosomes. Figures 1(g)–1(i) show the normal microscopy images, abnormal microscopy images, and chromosome fluorescent intensity, respectively.

Based on the method described above, we succeed in discriminating the normal and lung cancer cells according to the intensity of the chromosome fluorescence [Fig. 1(j)] in the map. In the middle of the chart, there is a normal zone between the red-dotted lines: the top and bottom red-dotted lines represent the intensity of the chromosome fluorescence to be 1000 and 750, respectively. If the intensity of the measured fluorescence lies beyond this region, then the cell is likely to be abnormal. An abnormal chromosome number may suggest that the cell is cancerous.

B. Map Validation by Detection of Abnormal Spermiogenesis in Male Mice

In order to prove that our detection method can distinguish the number of chromosomes in a single cell, we use reproductive cells of male mice which have various chromosome numbers due to abnormal spermiogenesis. The reproductive cells with a normal or an abnormal number of chromosomes come from our research partner (Shanghai Key Lab of Veterinary Biotechnology, School of Agriculture and Biology, Shanghai Jiao Tong University) [27]. As shown in Figs. 2(a)–2(c), we obtain haploid, diploid, and tetraploid sperm cells. Flow cytometry evaluates the separation of different testicular reproductive cells. The separations of cells are based on their sizes. The reproductive cells (haploid, diploid, and tetraploid sperm cells) are prepared separately in a suitable concentration ($1–10^2 \ \mu L^{-1}$) and injected into the sample cavity of the waveguide. Samples are washed with cold PBS three times and mixed with 3.7% formaldehyde at room temperature (RT) for 20 min followed by rinsing with phosphate buffer solution. Cells are permeabilized with PBS containing 0.5% Triton X-100 for 8 min. Then, we show the enhancement of the fluorescence from the chromosome in our waveguide, as shown in Figs. 2(d)–2(j).

Figures 2(d)–2(f) show the fluorescence microscope $\times 10^3$ imaging of different germ cells. The chromosomes are dyed by DAPI in the cells. Figures 2(g)–2(i) show the intensity of the fluorescence at the coupling angles when single haploid, diploid, and tetraploid sperm cells are injected into the waveguide, respectively. The central fluorescent wavelength is always 540 nm, and the value of the fluorescent peak is 923, 2005, and 3680 for a single haploid, diploid, and tetraploid sperm cell,
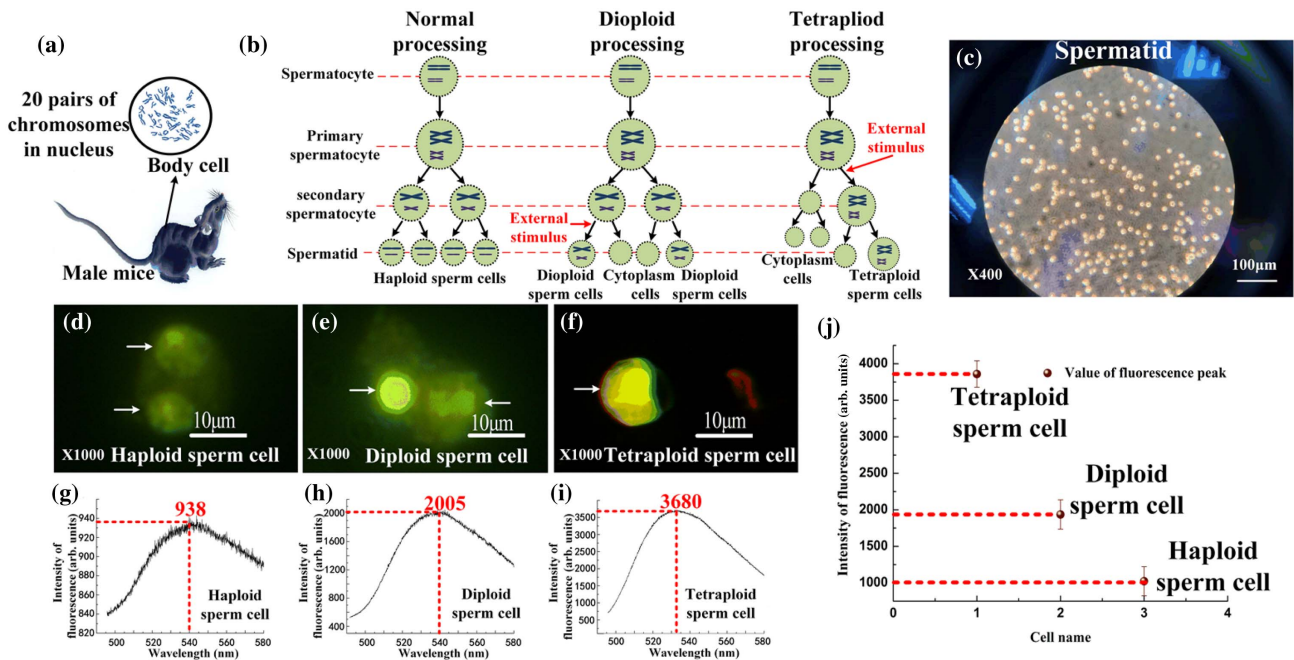

Fig. 2. Experimental results show that the mouse's chromosome number changes in the sperm cells. (a) Chromosome numbers of male mice. (b) Haploid sperm cells, diploid sperm cells, tetraploid sperm cells, and cytoplasm cells can be obtained from male mice spermatocyte stem cells during development and differentiation. (c) Haploid, diploid, tetraploid sperm cells, and cytoplasm cells imaged by microscope. (d)–(f) are fluorescent microscope imaging of the haploid, diploid, and tetraploid sperm cells, respectively. (g)–(i) Fluorescent intensity of the haploid, diploid, and tetraploid sperm cells, respectively. (j) Value of fluorescence peak of the haploid, diploid, and tetraploid sperm cells.

respectively [Fig. 2(j)]. Obviously, the fluorescent intensities can distinguish the number of chromosomes in a single cell.

C. Map Application *in vivo* Investigation of Therapy of Cancer

In the validation above, we find that the method based on our strong coupling waveguide can detect chromosomal abnormalities. Moreover, it can be further used to precisely monitor the process of cancer therapy. As shown in Fig. 3, the *in vitro* results demonstrate that our optical fluorescence detection map exhibits a strong and specific ability to distinguish cancer and normal cells via chromosome fluorescence. It is necessary to employ this method for *in vivo* studies of cancer therapy. In this experiment, 4T1 tumor-bearing mice (Laboratory of Regeneromics, School of Pharmacy, Shanghai Jiao Tong University) are used. Serial coronal PET/CT (positron emission tomography/ computed tomography) images of the 4T1 tumor-bearing mice at different time points of post-injection of the targeted drug are shown in Figs. 3(a) and 3(b). Tumors are indicated by the yellow arrowheads. After the targeted drug in cancer therapy [Fig. 3(a)], the tumor can no longer be seen via PET/CT imaging as shown in Fig. 3(b).
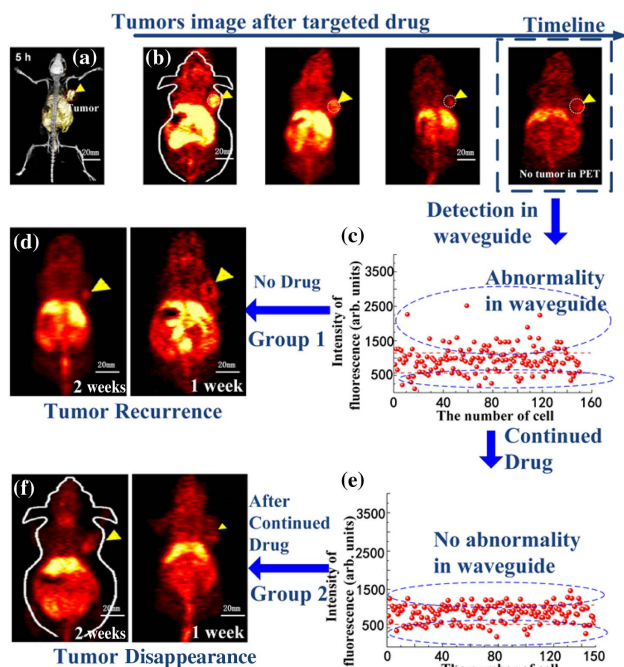
Meanwhile, we detect the cells from mice after therapy via our waveguide. The intensity of the chromosome fluorescence after therapy is shown in Fig. 3(c). The fluorescent data show some cells are in the abnormal zone (the top and bottom dotted lines above 1100 or below 500). Then, a proportion of these mice after therapy labeled as Group 1 are bred in highly controlled research environments for 1 week or more. The PET/ CT images after 1 week [Fig. 3(d)] demonstrate that tumors recur. And another part of these mice labeled as Group 2 are with continued drug under continuous monitoring until the data of the chromosome fluorescence intensity [Fig. 3(e)] are between the dotted lines (normal region), which represents tumors are completely killed in our fluorescence detection map. Observation is continued for 1 and 2 weeks after treatment. PET/CT images after 1 and 2 weeks [Fig. 3(f)] show that the tumors disappear in Group 2. In brief, the precise and easy diagnosis of abnormal cells is useful to cancer therapy. The results show that our ultrasensitive detection of an abnormal chromosome number is useful in cancer monitoring and treatment.

3. DISCUSSION

This work reports a fluorescence detection map which can detect a single cancer cell in real time via a strong coupling waveguide. In our work, the weak intensity of the fluorescence has been enhanced by the resonance with a UOM in the waveguide, resulting in the chromosome fluorescence of a single live cell being able to be identified without a high-resolution microscope. Based on the above, we propose the method by detecting the NSCLC, which can be applied to monitor the chromosomal abnormalities. Subsequently, the different testicular reproductive cells including haploid, diploid, and tetraploid sperm cells have been distinguished with the map. According to the *in vivo* experiments in mice, we find that the method can improve the chance of killing any remaining cancer cells to prevent the cancer from recurrence after cancer therapy, facilitating personalized cancer diagnosis and therapy. The single live cell at adjacent points after treatments for cancer can be monitored in real time by the waveguide in order to monitor the metastasis of the tumor in time. Moreover, for distant points the waveguide can be used as an adjuvant device to the cancer diagnosis, which possesses sensitive detection ability to compensate the shortcoming of existing medical conditions. Early and precise cancer diagnosis can substantially improve patient surviving due to our real-time ultrasensitive detection. The researchers, who have been working diligently to find a personalized cure for cancer, can get a useful and new way to monitor and treat cancers.

Fig. 3. Application of the fluorescence detection map with personalized cancer treatment to optimize therapeutic results. (a) Representative PET/CT and PET images of mice in the three groups at 5 h post-injection. All of the data represent three mice per group [26]. (b) Serial coronal PET images of 4T1 tumor-bearing mice at different time points of post-injection of the targeted drug; tumors are indicated by yellow arrowheads. (c) Chart of intensity of chromosome fluorescence after targeted drug in cancer therapy. There is no tumor in the mice by PET imaging. (d) PET images of Group 1 mice after cancer therapy without continued medication. The tumor recurrence is captured by PET 2 weeks after therapy. (e) Continued drug until the data of chromosome fluorescence intensity are between the dotted lines. (f) No tumor recurrence in Group 2 mice with continued drug in PET images under 1 and 2 weeks of observation.

4. MATERIALS AND METHODS

Authors claim: all applicable institutional and national guidelines for the care and use of animals were followed.

A. Strong Coupling Waveguide and Experimental System

The optical setup is illustrated in Fig. 4(a). The system is relatively simple due to the free space coupling technique. A computer-controlled $\theta/2\theta$ goniometer is applied for the

accurate angular scanning of the incident light to ensure efficient energy coupling. The size of the rectangular sample channel is 10 mm × 4 mm × 0.4 mm. All of the parts are optically contacted with excellent parallelism. A CCD (uEye Cockpit) is used to record signal data collected by closeup lenses perpendicular to the reflected light. In our approach, a photodiode monitors the variation of the reflected light intensity. The details are presented in Figs. 4(b) and 4(c). Figure 4(b) shows the diagram of the microsyringe. And the structure of the metal-cladding optofluidic waveguide is indicated in Fig. 4(c). Figures 4(d) and 4(e) show the details about attenuating the total reflection absorption peak (ATR). In experiments, the flow velocity is 10 μL/s, and the time interval of the recorded data is $\Delta t = 1$ min. After passing through a collimating system, a collimated beam with a 473 nm (CW) and 15 mW laser is coupled to the metal-cladding layer of the waveguide which rotates with the goniometer to excite the UOMs. After reaching the coupling angle θ_i, more than 99% incident light will be coupled into the waveguide. Therein, the effective index N_{eff} of the waveguide is between 0 and 1 due to the symmetrical metal cladding, the result of which is that the light can still be trapped in the waveguide layer without leakage. The liquid with a low refractive index is injected into the waveguide interlayer, so that the interaction between light and matter can be fully achieved in the waveguide. Meanwhile, the stimulation results show a molecular structure or weight change in the sample, corresponding to a change of refractive index $\sim 10^{-6}$, which will consequently generate a 0.012° angle shift as shown in Fig. 4(e).

As shown in Fig. 2(j), the different number of chromosomes can be detected by the intensity of the fluorescence change in the waveguide with a sperm cell suspension. But, if the suspension is mixed with impurities, just the detection of the refractive index may fail to distinguish the number of the chromosomes in the cell. Therefore, a method to achieve specific signals from

the chromosomes in the waveguide is needed to distinguish a single normal cell and an abnormal one. The fluorescence of the chromosome is a specific signal, and the intensity of the fluorescence is related to the number of chromosomes.

As shown in Fig. 5, we detect the intensity of the fluorescence at coupling angles $\theta_i = 0.41°$, $0.43°$, and $0.45°$, when the haploid, diploid, and tetraploid sperm cells are injected into the waveguide, respectively. As indicated in Fig. 5(a), the incident light knocks at the top of the waveguide at the coupling angle, and there is light power that was coupled into the waveguide. Thus, black lines are present on the reflected spots captured by the CCD. More detailed information about the incident light and reflected light is provided in Fig. 5(b). The fluorescent intensity remains stable at $\theta_i = 0.41°$, $0.43°$, and $0.45°$ [Fig. 5(c)]. Furthermore, the haploid, diploid, and tetraploid sperm cells can still be distinguished via detection of the fluorescent intensity.

B. Mouse Sperm Cell Preparation and the Separation of Different Testicular Cells

The mouse sperm used was previously described [28,29]. Briefly, KunMing mice (Shanghai Laboratory Animal Center of the Chinese Academy of Sciences) were used in this study. Animal experiments were performed according to the institutional guidelines for ethics (Approval number 86/609/EEC-24/11/86). All of the experimental procedures were approved by the Animal Ethics Committee of Shanghai Jiao Tong University (No. IACUC-2018-010). The housing facility is a barrier housing facility, and it is maintained according to the national standards contained in "Laboratory Animal-Requirements of Environment and Housing Facilities" (GB 14925-2001). The care of laboratory animals and the animal experimental operation conformed to the "Beijing Administration Rule of Laboratory Animals."

We used 10 cages (at least) of newborn male mice in each experiment, and the number of newborn male mice was more than 50. Newborn male mice were randomly divided into two
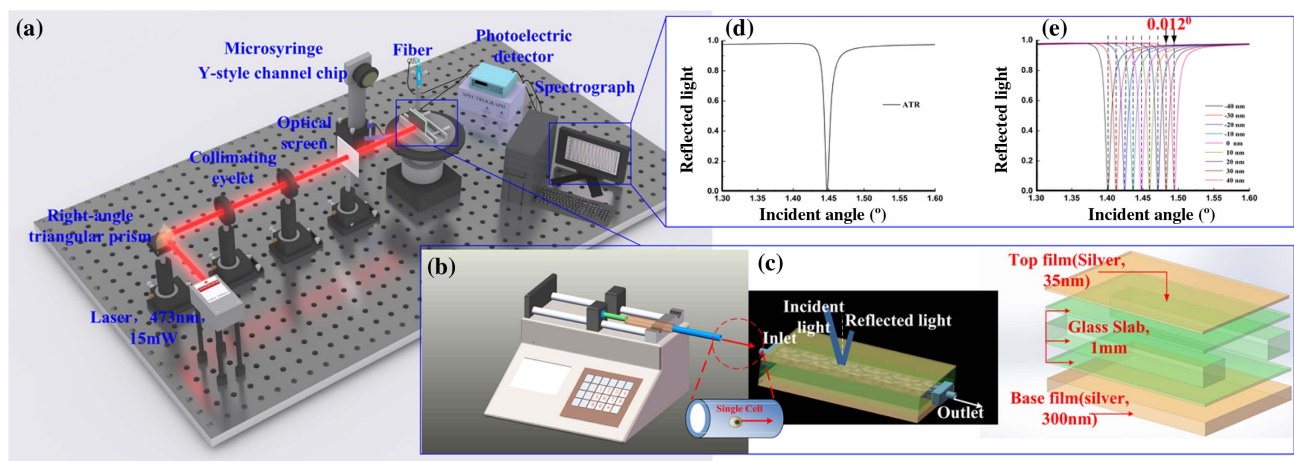

Fig. 4. Experiment system and the structure declaration of waveguide. (a) Experimental setup, (b) diagram of microsyringe, (c) structure of the waveguide. Five layers from top to bottom: a 0.3-mm-thick glass slide with 35 nm silver at the top, a 10 mm × 4 mm rectangular channel embedded in a 0.4-mm-thick glass slab working as sample container in the guiding layer, and another 0.3-mm-thick glass coated with 300-nm-thick silver at the bottom of the structure. These parts are optically contacted together and parallel to each other. Light is coupled into the sample channel of the fluidic waveguide. (d) The guided-wave absorbent peak (attenuating total reflection absorption peak, ATR) at coupling angle; 99% of the incident light is coupled into waveguide. (e) The coupling angle shift is due to the refractive index or the thickness of the waveguide layer.
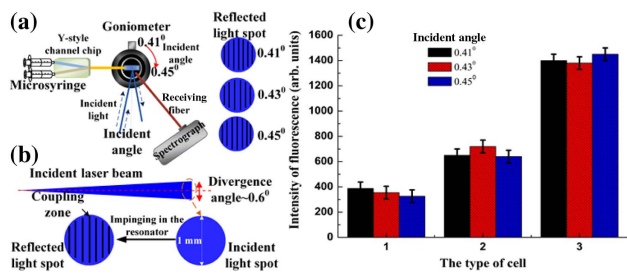
Fig. 5. Detection of fluorescent intensity system and stability. (a) Detection system for intensity of chromosome fluorescence. (b) Incident laser beam and divergence angle ~0.6°, incident light spot, and reflected light spot. (c) The coupling angle is different when the number of the chromosome is different in the cell. The incident angles are 0.41°, 0.43°, and 0.45°, and the numbers 1, 2, and 3 represent haploid, diploid, and tetraploid sperm cells; the intensity of fluorescence remains stable at 0.41°, 0.43°, and 0.45°.

groups and were caged separately. Ear cropping was used to identify the Pd-treated group. $PbCl_2$ (1.5 mg/kg BW [30,31]) was administered in the treated groups via intraperitoneal injection once every 2 days from postnatal days 10 to 60. The control groups were injected with the same volume of normal saline. All of the experiments were repeated three times. Based on a previous study of reproductive system development [32], we selected postnatal days 20, 40, and 60 to indicate the different developmental stages. The testes from the mice in each group were dissected and placed in 1 mL PBS to release the reproductive cells, and the tissues were removed and washed with PBS after 15 min.

C. 4T1 Murine Breast Cancer Model
To generate the 4T1 tumor model, 4–5-week-old female Qui Gue TM-PDX mice were purchased from JNO (Jennio-bio, Guangzhou, China). Tumors were established by subcutaneously injecting 2×10^6 cells which were suspended in 100 μL of 1:1 mixture of RPMI 1640 and matrigel (BD Biosciences, Franklin Lake, NJ) into the front flank of mice. The tumor sizes were monitored every other day by CT, and the animals were subjected to *in vivo* experiments when the tumor diameter was over 5 mm.

D. PET and PET/CT Imaging
PET and PET/CT scans at various time points were done postinjection using a microPET/microCT Inveon rodent model scanner (Siemens Medical Solution USA, Inc.) with 2 μm resolution. The scan space was 80 mm × 200 mm. Moreover, the image reconstruction and the ROI analysis of the PET data were presented as a percentage injected dose per gram of tissue (% ID/g). Tumor-bearing mice were each injected with 5–10 MBq of contrast agent via the tail vein before serial PET scans.

E. Histology
Frozen tissue slices (7 μm thickness) were fixed with cold acetone and stained for endothelial marker CD31 through the use of a rat antimouse CD31 antibody and a Cy3-labeled donkey antirat IgG. The tissue slice was also incubated with 2 μg/mL of acridine-orange-labeled goat antihuman IgG for

visualization of the chromosome. All of the images were acquired with a DYF-880 fluorescent microscope.

F. Cell Culture
The cells were cultured in Dulbecco's modified Eagle's medium (DMEM) containing 10% FBS, penicillin (100 U/mL), and streptomycin (100 μg/mL). The cells were incubated in a humidified atmosphere with 5% CO_2 at 37°C.

G. Other Materials
Acridine orange and Cy3-labeled secondary antibodies were purchased from Sinopharm Chemical Reagent Co., Ltd. (Shanghai, China). Absolute ethanol, sodium chloride (NaCl), and doxorubicin hydrochloride (DOX) were purchased from Fisher Scientific. Water and all buffers were of Millipore grade and pretreated with a Chelex 100 resin to ensure that the aqueous solution was free of heavy metals. All of the chemicals were used as received without further purification.

Disclosures. The authors declare no conflicts of interest.

Data Availability. No data were generated or analyzed in the presented research.

†These authors contributed equally to this paper.

REFERENCES

1. D. Hanahan and R. A. Weinberg, "The hallmarks of cancer," Cell **100**, 57–70 (2000).
2. S. I. Grivennikov, F. R. Greten, and M. Karin, "Immunity, inflammation, and cancer," Cell **140**, 883–899 (2010).
3. B. B. Aggarwal, R. V. Vijayalekshmi, and B. Sung, "Targeting inflammatory pathways for prevention and therapy of cancer: short-term friend, long-term foe," Clin. Cancer Res. **15**, 425–430 (2009).
4. K. Raghu and R. A. Weinberg, "The basics of epithelial-mesenchymal transition," J. Clin. Invest. **119**, 1420–1428 (2010).
5. J. Bollrath, T. J. Phesse, V. Burstin, T. Putoczki, M. Bennecke, T. Bateman, T. Nebelsiek, T. Lundgren-May, O. Canli, S. Schwitalla, V. Matthews, R. M. Schmid, T. Kirchner, M. C. Arkan, M. Ernst, and F. R. Greten, "gp130-mediated Stat3 activation in enterocytes regulates cell survival and cell-cycle progression during colitis-associated tumorigenesis," Cancer Cell **15**, 91–102 (2009).
6. J. F. Bosset, L. Collette, G. Calais, L. Mineur, P. Maingon, R. J. Ljiljana, A. Daban, E. Bardet, A. Beny, and J. C. Ollier, "Chemotherapy with preoperative radiotherapy in rectal cancer," N. Engl. J. Med. **355**, 1114–1123 (2006).

7. C. M. Ribic, D. J. Sargent, M. J. Moore, S. N. Thibodeau, A. J. French, R. M. Goldberg, S. R. Hamilton, L. P. Pierre, R. Gryfe, L. E. Shepherd, D. Tu, M. Redston, and S. Gallinger, "Tumor microsatellite-instability status as a predictor of benefit from fluorouracil-based adjuvant chemotherapy for colon cancer," N. Engl. J. Med. **349**, 247–257 (2003).

8. H. M. Quah, J. Chou, F. Gonen, M. Shia, J. Schrag, D. Landmann, R. Guillem, G. Paty, J. Temple, P. Wong, and B. Weiser, "Identification of patients with high-risk stage II colon cancer for adjuvant therapy," Dis. Colon. Rectum. **51**, 503–507 (2008).

9. G. P. Dunn, C. M. Koebel, and R. D. Schreiber, "Interferons, immunity and cancer immunoediting," Nat. Rev. Immunol. **6**, 836–848 (2006).

10. S. Benchimol, A. Fuks, S. Jothy, N. Beauchemin, S. Kinji, and C. P. Stanners, "Carcinoembryonic antigen, a human tumor marker, functions as an intercellular adhesion molecule," Cell **57**, 327–334 (1989).

11. P. Nazerian, V. Volpicelli, B. Gigli, B. Zanobetti, I. Ermini, and S. Grifoni, "Accuracy of lung ultrasound for the diagnosis of consolidations when compared to chest computed tomography," Crit. Ultrasound J. **7**, A13 (2015).

12. Y. Cai, W. Si, W. Huang, P. Chen, J. Shao, and X. Dong, "Organic dye based nanoparticles for cancer phototheranostics," Small **14**, 1704247 (2018).

13. A. B. Chinen, C. M. Guan, J. R. Ferrer, S. N. Barnaby, T. J. Merkel, and C. A. Mirkin, "Nanoparticle probes for the detection of cancer biomarkers, cells, and tissues by fluorescence," Chem. Rev. **115**, 10530–10574 (2015).

14. P. V. Shanta, D. D. Stuart, and Q. Cheng, "Graphene oxide-nanocarriers for fluorescent sensing of calcium ion accumulation and direct assessment of ion-induced enzymatic activities in cells," ACS Appl. Nano Mater. **2**, 5594–5603 (2019).

15. J.-A. Huang, V. Caprettini, Y. Zhao, G. Melle, N. Maccaferri, L. Deleye, X. Zambrana-Puyalto, M. Ardini, F. Tantussi, M. Dipalo, and F. D. Angelis, "On-demand intracellular delivery of single particles in single cells by 3D hollow nanoelectrodes," Nano Lett. **19**, 722–731 (2019).

16. Q. Shi and R. King, "Chromosome nondisjunction yields tetraploid rather than aneuploid cells in human cell lines," Nature **437**, 1038–1042 (2005).

17. R. Fodde, J. Kuipers, C. Rosenberg, R. Smits, M. Kielman, C. Gaspar, H. V. E. Johan, C. Breukel, J. Wiegant, R. H. Giles, and H. Clevers, "Mutations in the APC tumour suppressor gene cause chromosomal instability," Nat. Cell Biol. **1**, 433–438 (2006).

18. E. Hernando, Z. Nahlé, G. Juan, E. D. Rodriguez, M. Alaminos, M. Hemann, L. Michel, V. Mittal, W. Gerald, R. Benezra, S. W. Lowe, and C. C. Cardo, "Rb inactivation promotes genomic instability by uncoupling cell cycle progression from mitotic control," Nature **430**, 797–802 (2004).

19. P. V. Jallepalli, I. C. Waizenegger, F. Bunz, L. Sabine, M. R. Speicher, J. M. Peters, K. W. Kinzler, B. Vogelstein, and C. Lengauer, "Securin is required for chromosomal stability in human cells," Cell **105**, 445–457 (2001).

20. F. Chen, Z. Cao, Q. Shen, and Y. Feng, "Optical approach to angular displacement measurement based on attenuated total reflection," Appl. Opt. **44**, 5393–5397 (2005).

21. Y. Wang, Z. Cao, T. Yu, H. Li, and Q. Shen, "Enhancement of the superprism effect based on the strong dispersion effect of ultra-high-order modes," Opt. Lett. **33**, 1270–1276 (2008).

22. H. Li, Z. Cao, H. Lu, and Q. Shen, "Free-space coupling of a light beam into a symmetrical metal-cladding optical waveguide," Appl. Phys. Lett. **83**, 2757–2759 (2003).

23. W. Yi, Z. Cao, H. Li, Q. Shen, W. Yuan, and P. Xiao, "Tunable polarization beam splitting based on a symmetrical metal-cladding waveguide structure," Opt. Express **17**, 13157–13167 (2009).

24. H. Dai, C. Yin, X. Ye, B. Jiang, M. Ran, Z. Cao, and X. Chen, "A possible pathogenetic factor of sickle-cell disease based on fluorescent analysis via an optofluidic resonator," Sci. Rep. **7**, 3174 (2017).

25. J. Bei, H. Dai, and X. Chen, "Enhancement of stimulated emission by a metallic optofluidic resonator," Photon. Res. **6**, 597–600 (2018).

26. Q. Deng, X. Yu, S. Deng, H. Ye, Y. Zhang, W. Han, J. Li, and Y. Yu, "Midkine promotes articular chondrocyte proliferation through the MK-LRP1-nucleolin signaling pathway–sciencedirect," Cell. Signal. **65**, 109423 (2020).

27. Q. Yang, X. Liu, J. Chen, Y. Wen, H. Liu, Z. Peng, R. Yeerken, L. Wang, and X. Li, "Lead-mediated inhibition of lysine acetylation and succinylation causes reproductive injury of the mouse testis during development," Toxicol. Lett. **318**, 30–43 (2020).

28. X. Li, L. Wang, Y. Li, J. Fu, L. Zhen, Q. Yang, S. Li, and Y. Zhang, "Tyrosine phosphorylation of dihydrolipoamide dehydrogenase as a potential cadmium target and its inhibitory role in regulating mouse sperm motility," Toxicology **357–358**, 52–64 (2016).

29. Q. Yang, P. Li, Y. Wen, S. Li, J. Chen, X. Liu, L. Wang, and X. Li, "Cadmium inhibits lysine acetylation and succinylation inducing testicular injury of mouse during development," Toxicol. Lett. **291**, 112–120 (2018).

30. D. S. P. Fabricia, M. A. S. Diamante, and D. Heidi, "Testis response to low doses of cadmium in Wistar rats," Int. J. Exp. Pathol. **91**, 125–131 (2010).

31. J. Zhang, H. A. S. Cao, Y. Zhang, Y. Zhang, J. Ma, J. Wang, Y. Gao, X. Zhang, F. Zhang, and L. Chu, "Nephroprotective effect of calcium channel blockers against toxicity of lead exposure in mice," Toxicol. Lett. **218**, 273–280 (2013).

32. A. R. Bellvé, C. F. Millette, Y. M. Bhatnagar, and D. A. O'Brien, "Dissociation of the mouse testis and characterization of isolated spermatogenic cells," J. Histochem. Cytochem. **25**, 480–494 (1977).